

# Origin of defect tolerance in InAs/GaAs quantum dot lasers grown on silicon

Zizhuo Liu, Constanze Hantschmann, Mingchu Tang, Ying Lu, Jae-Seong Park, Mengya Liao, Shujie Pan, Ana Sanchez, Richard Beanland, Mickael Martin, Thierry Baron, Siming Chen, Alwyn Seeds, Richard Penty, Ian White, and Huiyun Liu

**Abstract**—High-performance III-V quantum-dot lasers monolithically grown on Si substrates have been demonstrated as a promising solution to realise Si-based laser sources with very low threshold current density, high output power and long lifetime, even with relatively high density of defects due to the material dissimilarities between III-Vs and Si. On the other hand, although conventional III-V quantum-well lasers grown on Si have been demonstrated after great efforts worldwide for more than 40 years, their practicality is still a great challenge because of their very high threshold current density and very short lifetime. However, the physical mechanisms behind the superior performance of silicon-based III-V quantum-dot lasers remain unclear. In this paper, we directly compare the performance of a quantum-well and a quantum-dot laser monolithically grown on on-axis Si (001) substrates, both experimentally and theoretically, under the impact of the same density of threading dislocations. A quantum-dot laser grown on a Si substrate with a high operating temperature (105 °C) has been demonstrated with a low threshold current density of 173 A/cm<sup>2</sup> and a high single facet output power >100 mW at room temperature, while there is no lasing operation for the quantum-well device at room temperature even at high injection levels. By using a rate equation travelling-wave model, the quantum-dot laser's superior performance compared with its quantum well-based counterpart on Si is theoretically explained in terms of the unique properties of quantum dots, i.e., efficient carrier capture and high thermal energy barriers preventing the carriers from migrating into defect states.

**Index Terms**—quantum dot lasers, silicon photonics, Semiconductor growth

## I. INTRODUCTION

SI-BASED photonic integrated circuits (PICs) are expected to meet the demands of the ever growing increase in data traffic by providing an efficient data transmission method via optical interconnects integrated on the Si platform [1]. Moreover, Si-based PICs have the potential to reduce the cost to few cents per gbits<sup>-1</sup> compared with InP-based state-of-art optical transceiver [2]. An efficient and reliable Si-based laser

is the key component for the deployment of Si-based PICs [3]. Although great efforts have been made on the development of group IV-based lasers [3-6], fabricating and integrating these light sources with other well-established photonic components is still challenging due to the extremely high threshold current densities and restricted device performance arising from the indirect bandgap of Si and Ge. Integrating III-V lasers on Si or SOI platforms, on the other hand, is an attractive approach, because it enables Si-based PICs to leverage the superior electrical and optical properties of III-V semiconductors. While both monolithic and heterogeneous III-V integration concepts have been demonstrated [7-8], growing GaAs- and InP-based lasers directly on Si platform is considered the more promising method for realizing dense and low-cost integration of III-V lasers on Si in the longer term.

The major challenges of heteroepitaxial growth of GaAs or InP on Si are the antiphase domains (APDs) and threading dislocations (TDs) due to the polar on non-polar and lattice-mismatched heteroepitaxial growth, respectively. Over the past years, however, researchers have developed methods to grow single-domain III-V materials on offcut and on-axis Si substrates successfully, especially GaP and GaAs on Si [9-11], which in turn has led to the successful demonstration of telecommunication wavelength lasers on GaP/Si and GaAs/Si virtual substrates [12-19]. In addition to the APD issue, the high density of TDs originating from the lattice mismatch between Si and III-V materials, 4 % and 7 % for GaAs and InP, respectively, results in a significant degradation of the laser performance due to the formation of nonradiative recombination centers [20-21]. It has been shown that strained layer superlattices (SLSs) act as effective defect filter layers (DFLs) being able to reduce the TD density from 10<sup>10</sup> cm<sup>-2</sup> to below 10<sup>6</sup> cm<sup>-2</sup> [16], yet even these reduced defect densities are still orders of magnitude higher than those in III-V lasers grown on native substrates [22].

The authors acknowledge financial support from UK EPSRC under Grant No. EP/P000886/1 and EPSRC National Epitaxy Facility. SC thanks the Royal Academy of Engineering for funding his Research Fellowship. CH thanks Qualcomm Inc. for PhD funding. The first two authors contributed equally to this work. (corresponding author: Mingchu Tang, Huiyun Liu)

Z. Liu, M. Tang, Y. Lu, J. Park, M. Liao, S. Pan, S. Chen, A. Seeds and H. Liu are with the Department of Electronic and Electrical Engineering, University College London, Torrington Place, London, WC1E 7JE, United Kingdom. (e-mail: [mingchu.tang.11@ucl.ac.uk](mailto:mingchu.tang.11@ucl.ac.uk); [Huiyun.liu@ucl.ac.uk](mailto:Huiyun.liu@ucl.ac.uk)).

C. Hantschmann, R. Penty and I. White are with the Centre for Photonic Systems, Department of Engineering, University of Cambridge, 9 JJ Thomson Avenue, Cambridge CB3 0FA, United Kingdom.

A. Sanchez and R. Beanland are with the Department of Physics, University of Warwick, Coventry, CV4 7AL, United Kingdom.

M. Martin and T. Baron are with Univ. Grenoble Alpes, CNRS, CEA-LETI, MINATEC, LTM, F-38054 Grenoble, France

Since quantum wells (QWs) are the gain medium of choice for most commercial laser diode applications, great effort has been devoted to developing monolithic III-V QW lasers on Si over the past 40 years. However, even at moderate dislocation densities, only poor device performance has been obtained with operating lifetimes not exceeding  $\sim 200$  hours [23]. InAs/GaAs quantum dots (QDs), on the other hand, have recently been proposed to be a more suitable gain medium for direct growth on Si, showing impressive laser performance in terms of a very low threshold current density of  $62.5 \text{ Acm}^{-2}$  and a record lifetime of 3,001,402 hours [16,18,19]. What is more, these QD lasers have demonstrated good lasing characteristics even at high TD densities of the order up to  $10^8 \text{ cm}^{-2}$  [18]. The advantage of QD over QW structures on Si has been confirmed in systematic experimental studies on the lifetimes of III-V QD laser on Si with different densities of TDs in the active region. Recently, we have reviewed the progress of InAs/GaAs QD lasers monolithically grown on group-IV platforms [24], however, the key physical mechanisms behind the high performance of Si-based III-V QD lasers, which is comparable to record values of QD lasers on native substrates, have not been clearly identified yet. In addition, the lack of high-performance Si-based QW lasers raises the question of to what value must the defect density be reduced, or whether QW active regions may not be suitable for direct III-V laser growth on Si at all. For this reason, it is necessary to make a direct comparison to evaluate the effect of TDs on QD and QW active regions in Si-based lasers, and to explain the nature behind higher performance of QD laser grown on Si.

In this paper, we present an experimental and theoretical study on the impact of TDs on III-V QD and QW lasers, monolithically grown on on-axis Si substrates under the same conditions. For the QD laser, a continuous-wave (cw) threshold current density as low as  $173 \text{ Acm}^{-2}$  has been obtained at room temperature, with an output power exceeding 200 mW. The QW device, in stark contrast, does not show any lasing at all, even under pulsed current injection up to  $2 \text{ kAcm}^{-2}$ . To explain these results at a more fundamental level, a rate equation travelling-wave approach including a phenomenological term to model enhanced non-radiative recombination induced by TDs is used. Our calculations show that ultrafast QD carrier capture as well as effective carrier confinement in the QD states enable lasers with QD active regions to show lasing up to higher dislocation densities than for QW lasers.

## II. CRYSTAL GROWTH AND DEVICE FABRICATION

An APD-free 400 nm GaAs layer was grown on a 300 mm Si on-axis (001) substrate to form a GaAs/Si virtual substrate by using MOCVD with two-step growth [10]. Then, the 400 mm GaAs/Si virtual substrate was diced into 2-inch wafers and transferred into a Veeco GEN930 MBE chamber to grow the laser structure. III-V buffer layers including a 300 nm GaAs layer and four sets of DFLs were grown on the GaAs/Si virtual substrate in order to suppress the propagation of TDs generated at the GaAs/Si interface. Each set of DFL consists of five periods of 10 nm/10 nm  $\text{In}_{0.15}\text{Ga}_{0.85}\text{As}/\text{GaAs}$  SLSs and a 300 nm GaAs spacing layer. An active region was embedded within

two layers of 1500 nm  $\text{Al}_{0.4}\text{Ga}_{0.6}\text{As}$  upper and lower cladding layers. To compare the performance of QW and QD lasers on Si substrates, two types of active region, InAs/GaAs dot-in-well (DWELL) and InGaAs/GaAs multi-quantum well (MQW), were grown. The QD active region consists of five layers of DWELL structure including three monolayers (MLs) of InAs QD grown on 2 nm  $\text{In}_{0.15}\text{Ga}_{0.85}\text{As}$  QW and capped with 6 nm  $\text{In}_{0.15}\text{Ga}_{0.85}\text{As}$  at  $510^\circ\text{C}$ . Adjacent DWELL layers are separated by a 5 nm low-temperature GaAs spacer layer and a 35 nm high-temperature GaAs spacer layer [25]. In contrast, the MQW active region comprised five layers of low-temperature grown 8 nm  $\text{In}_{0.15}\text{Ga}_{0.85}\text{As}$  QWs each spaced by a 40 nm GaAs spacer layer. A highly doped p-type GaAs contact layer completed the

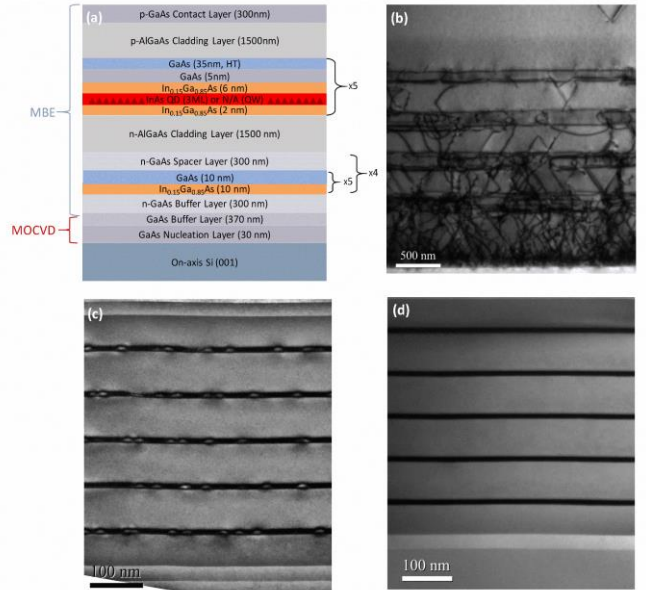


Fig. 1. (a) Schematic diagram of InAs/GaAs QD and  $\text{In}_{0.15}\text{Ga}_{0.85}\text{As}/\text{GaAs}$  QW laser monolithically grown on Si on-axis (001) substrate. Cross-sectional TEM images of (b), III-V buffer layers grown on on-axis Si substrate with 4 sets of  $\text{In}_{0.18}\text{Ga}_{0.82}\text{As}/\text{GaAs}$  SLSs DFLs and a 600 nm GaAs buffer layer. (c) 5 layers of DWELL structure and (d) 5 layers of  $\text{In}_{0.15}\text{Ga}_{0.85}\text{As}/\text{GaAs}$  MQW.

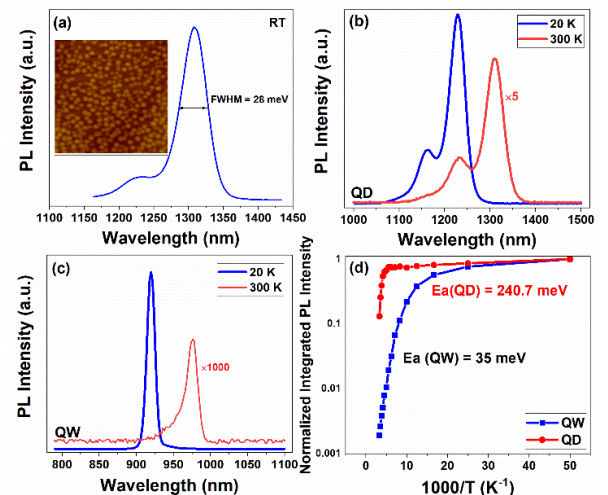


Fig. 2 (a) Room-temperature PL spectrum of QDs excited by a 635 nm red laser. Inset: AFM image of uncapped InAs/GaAs QDs grown on on-axis Si substrate. PL spectra at room temperature (300 K) and low temperature (20 K) of (b) the QD laser, and (c) the QW laser excited by a 532 nm green laser. (d) Temperature-dependent integrated PL intensities of the InAs/GaAs QD and InGaAs/GaAs QW lasers from the temperature region of 20 K to 300 K.

laser structure. Note that all QD and QW laser growth conditions were identical except for the active region growth.

Broad-area laser devices were fabricated using standard photolithography, wet etching, and metallization techniques. After forming a 50  $\mu\text{m}$  ridge and exposing the heavily doped n-type GaAs contacting layer by conventional wet etching, Ni/GeAu/Ni/Au (10/100/30/200 nm) and Ti/Au (40/400 nm) metal contact layers were deposited on the n-GaAs and the p-GaAs contacting layer, respectively. After thinning the Si substrates to around 120  $\mu\text{m}$ , the laser bars were cleaved into 3 mm long laser cavities, without high-reflection coatings. Finally, the bars were thermally bonded to a copper heatsink, and gold-wire bonding was applied for testing.

### III. RESULTS AND DISCUSSIONS

As shown in Fig. 1(a), the InAs/GaAs QD and InGaAs/GaAs QW laser structures were directly grown on on-axis Si (001) substrates. The active regions are composed of 5 layers of InAs/InGaAs dots-in-a-well (DWELL) or InGaAs/GaAs QWs separated by 50 nm GaAs spacer layers. To characterize the crystalline quality of the grown samples, various measurement techniques such as transmission electron microscopy (TEM), photoluminescence (PL) and atomic force microscopy (AFM) were performed. Fig. 1(b) presents a cross-sectional TEM image of four sets of  $\text{In}_{0.18}\text{Ga}_{0.82}\text{As}/\text{GaAs}$  SLSs DFLs and a 700 nm GaAs buffer layer grown on on-axis Si (001) substrate, indicating that the TDs are effectively eliminated by the strained-layers. A high TD density of  $1.0 \times 10^{10} \text{ cm}^{-2}$  is generated at the GaAs/Si interface due to the large lattice mismatch between the two materials. With the help of tensile and compressive strain introduced by the lattice mismatched

$\text{In}_{0.18}\text{Ga}_{0.82}\text{As}/\text{GaAs}$  strained-superlattice, however, the TDs are bent toward the edge side of the wafer due to the strain force between the SLSs. In addition, the in-situ thermal annealing promotes the TDs' motion and, hence, increases the possibility of TDs' meeting, leading to the elimination of the two respective TDs if their Burgers vectors are perpendicular. Eventually, a defect density reduced to approximately  $5 \times 10^7 \text{ cm}^{-2}$  is obtained after the four sets of DFLs. Visible defect-free DWELL and MQW regions are shown in Fig. 1(c) and (d), respectively.

The optical properties of optimized InAs/GaAs QDs grown on on-axis Si (001) substrate are presented in Fig. 2(a). A dot density of  $4 \times 10^{10} \text{ cm}^{-2}$  (inset) was obtained with a narrow full-width-half-maximum (FWHM) of 28 meV, centered at a wavelength of 1310 nm at room temperature. Temperature-dependent PL measurements were performed by using a 532-nm wavelength laser to excite the samples cooled by a cryogenic temperature controller from 300 K to 20 K, as shown in Fig. 2(b) and (c), respectively. The room temperature PL intensity of the QD sample is six times lower than the PL intensity at 20 K. On the other hand, the QW sample's PL intensity at 20 K is  $\sim 1000$  times higher than the PL intensity of the QW sample at room temperature. To estimate the thermal activation energy of the two samples, the integrated PL intensity (IPLI) is measured as a function of temperature, as shown in Fig. 2(d). The IPLI of the QD sample remains approximately constant up to 200 K, and then decreases by a factor of 10 up to room temperature. This behavior is typical for InAs/GaAs QDs and has been attributed to the higher thermal energy barrier for the carriers to escape from the QDs due to the discrete energy levels within QDs [26-27]. On the other hand, the IPLI of QW sample quenches slowly at low temperature and

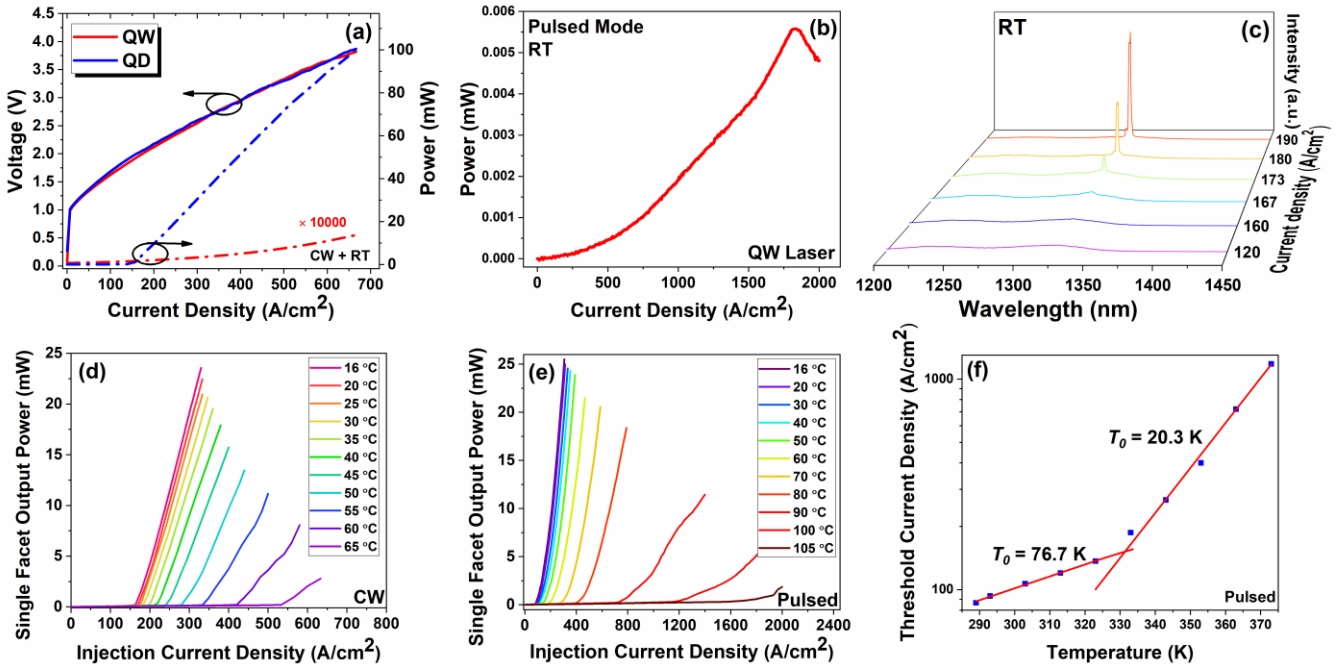


Fig. 3. (a) Room temperature  $L$ - $I$ - $V$  measurements of QD and QW lasers monolithically grown on on-axis Si (001) substrate under the same growth conditions. (b)  $L$ - $I$  measurement of the QW laser with higher injection current under pulsed mode at room temperature. (c) Lasing spectra of the QD laser with different injection current density indicating a threshold current density as low as 173  $\text{A}/\text{cm}^2$ . Temperature-dependent  $L$ - $I$  measurement of the QD laser under (d) continuous-wave mode and (e) pulsed mode. (f) Characteristic temperature measured under pulsed mode between 16  $^{\circ}\text{C}$  and 100  $^{\circ}\text{C}$ .

reduces dramatically above 50 K, which could be understood by the thermal carrier escape from QWs' continuum state [26]. As there are continuum states in QWs, small thermal energy will cause the carriers to escape from QWs. The PL quenching at high temperatures is fitted with the Arrhenius equation, giving thermal activation energies of about 240.7 meV and 35 meV for the QD and the QW sample, respectively. The significantly higher thermal activation energy observed for the QD sample contributes to its higher optical intensity at high temperatures, as carriers are well-trapped by the higher thermal barriers of QDs which prevents them from thermalizing into the wetting layer and barrier layer continuum, and then transferring to defect states [27].

Broad-area lasers were fabricated and cleaved then mounted on gold-plated copper heatsinks using indium–silver low-melting-point solder and gold-wire-bonded. Fig. 3(a) presents cw light-current-voltage ( $L$ - $I$ - $V$ ) measurements for the QD and QW laser at room temperature. The measured series resistances of the QD and QW lasers are very similar, corresponding to  $2.39 \pm 0.01 \Omega$  and  $2.38 \pm 0.02 \Omega$ , respectively. The QD laser shows a low threshold current density of  $173 \text{ Acm}^{-2}$  and a single-facet output power of 100 mW at an injection current of  $650 \text{ Acm}^{-2}$  without any rollover, whereas the QW laser produces negligible light output and does not show any lasing behaviour at all. Note that the measured maximum output power of the QD laser is limited by the current source used. Additional measurements up to higher injection currents under pulsed operation reveal a clear superlinear increase of the QW  $L$ - $I$  curve, as can be seen in Fig. 3(b), yet the output power rollover at  $\sim 1800 \text{ Acm}^{-2}$  seems to prevent the device from entering the lasing regime. For the given device geometries, these results give clear evidence of the superior lasing characteristics of the QD laser monolithically grown on Si compared with its QW-based counterpart, being in agreement with a similar experimental comparison of QD and QW laser structures grown on Si with a higher dislocation density of  $10^8 \text{ cm}^{-2}$  reported in [28]. Fig. 3(c) shows lasing spectra of the QD laser with different injection current densities from  $120 \text{ Acm}^{-2}$  to  $190 \text{ Acm}^{-2}$ , demonstrating lasing behavior at an injection current density of  $173 \text{ Acm}^{-2}$  and an emission wavelength of 1326.4 nm.

Temperature-dependent QD laser  $L$ - $I$  measurements are displayed in Fig. 3 (d) and (e) under cw mode and pulsed mode, respectively. The maximum operation temperature of the QD laser reaches  $65^\circ \text{C}$  under cw mode. In contrast, a maximum operation temperature of  $105^\circ \text{C}$  is obtained under pulsed mode. The characteristic temperature of the QD laser, measured under pulsed mode, is 76.7 K from  $16^\circ \text{C}$  to  $50^\circ \text{C}$ , and decreases to 20.3 K from  $60^\circ \text{C}$  to  $100^\circ \text{C}$  due to the carrier escape at high operation temperatures, as can be seen in Fig. 3 (f). It is worthwhile to note that, compared with our previous work, the performance of the QD laser monolithically grown on on-axis Si (001) substrate is significantly improved, which can be ascribed to the optimized QD and III-V growth conditions [13].

In order to understand the enormous performance disparity observed between the QW and QD structures, a rate equation traveling-wave model with one-dimensional spatial resolution

is used to simulate the impact of dislocations by including dislocation-dependent carrier loss. The following is a phenomenological approach aimed at explaining the observed behaviour qualitatively, considering only mid-bandgap defect states. Shallow traps in thermal equilibrium with the conduction and valence band are ignored as well as carrier re-emission from the defect states. It should also be noted that this approach does not consider device degradation due to dislocation climb, which is known to be a common failure mechanism in III-V QW lasers grown on Si and on native substrates [28-29]. The simulations therefore indicate the intrinsic QD and QW laser performance as a function of defect density at time zero.

The impact of TDs can be described as following. Carriers in the vicinity of a dislocation can migrate into the defect state, where they are likely to recombine non-radiatively [29-30]. Since this process involves carriers in the barrier layer (BL) and the wells in the instance of a QW laser, it becomes increasingly difficult to attain a population inversion in the presence of many dislocations. QDs, however, provide a lasing level safe from non-radiative recombination, as captured carriers cannot diffuse into defect states unless they thermalize back up into the wetting layer (WL) [31]. The total carrier lifetime is, therefore, written as

$$\tau_{nr,tot}^{-1} = \tau_{nr}^{-1} + \tau_{dis}^{-1} \quad (1)$$

where  $\tau_{nr}$  is the minority carrier lifetime in the absence of dislocations, and  $\tau_{dis}$  represents the non-radiative component as a function of the dislocation density  $\rho_{dis}$  [32-36]. To estimate  $\tau_{dis}$ , we consider the average spacing  $2/\sqrt{\pi\rho_{dis}}$  between two dislocations, corresponding to the dislocation-limited diffusion length  $L_{diff,dis}$ . The respective dislocation-dependent minority carrier lifetime is then given over the relationship to the diffusion constant  $D$  as [36]

$$\tau_{dis} = \frac{L_{diff,dis}^2}{D} \quad (2)$$

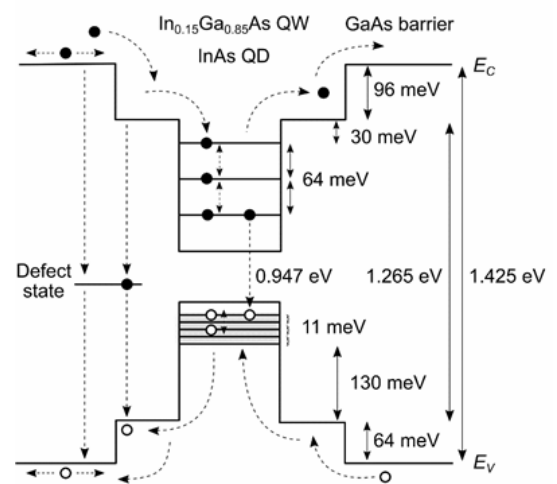


Fig. 4. Schematic one-dimensional real-space energy band diagram of the investigated InAs/GaAs QD lasers [19,37]. Non-radiative recombination processes via defect centers introduced by TDs propagating through the active region take place from the wetting layer/QWs and the barrier layer. Carriers confined in the QDs are not affected unless they thermalize out of the QD states. The respective energy band diagram for the InGaAs/GaAs QW lasers does not contain the QD structures but remains the same otherwise.

Additionally, it is considered that defect states saturate as higher carrier densities are reached [34].  $\tau_{dis}$  is, therefore, multiplied with a phenomenological saturation term  $(1 + n_{WL,BL}/n_{sat})$ , where  $n_{WL,BL}$  is the respective WL/QW or BL carrier density and the reference value  $n_{sat}$  is  $10^{18} \text{ cm}^{-3}$  [35]. The obtained values of  $\tau_{dis}$  differ for electrons and holes, which is a result of the different diffusion constants, as pointed out by *Andre et al.*[36]. For  $\rho_{dis} \gtrsim 7 \times 10^6 \text{ cm}^{-2}$ , for instance, the dislocation related electron lifetime according to (3) drops into the sub-nanosecond range, where it starts to affect the laser performance seriously, whereas for holes, this is only the case from  $\rho_{dis} \gtrsim 10^8 \text{ cm}^{-2}$ . This is a result of the faster interaction between electrons and dislocations due to the high electron mobility, which is in agreement with the short electron lifetimes that have been measured in epitaxial GaAs on non-native substrates [36]. However, it is currently not known if the defect states formed by TDs in III-V structures on Si behave acceptor- or donor-like, which will certainly affect the respective capture dynamics.

The InAs/GaAs QD laser is modelled as a system consisting of BL, WL, three confined electron QD states (GS, ES1, ES2) and five-hole QD levels (GS, ES1 – ES4), as illustrated schematically in Fig. 4 [37]. The electron rate equations are given as

$$\frac{dN_{BL}^e}{dt} = \frac{\eta I \Delta z}{e L} + \frac{N_{WL}^e f_{BL}^{e'}}{\tau_{esc}^{e'}} - \frac{N_{BL}^e f_{WL}^{e'}}{\tau_c^{e'}} - \frac{N_{BL}^e}{\tau_{nr}^{e'}} - \frac{N_{BL}^e}{\tau_{dis}^e} \quad (3)$$

$$\frac{dN_{WL}^e}{dt} = \frac{N_{BL}^e f_{WL}^{e'}}{\tau_c^{e'}} + \frac{N_{ES2}^e f_{WL}^{e'}}{\tau_{esc}^{e'}} - \frac{N_{WL}^e f_{BL}^{e'}}{\tau_{esc}^{e'}} - \frac{N_{WL}^e f_{ES2}^{e'}}{\tau_c^{e'}} - \frac{N_{WL}^e}{\tau_{nr}^{e'}} - \frac{N_{WL}^e}{\tau_{dis}^e} \quad (4)$$

$$\frac{dN_{ES2}^e}{dt} = \frac{N_{WL}^e f_{ES2}^{e'}}{\tau_c^{e'}} + \frac{N_{ES1}^e f_{ES2}^{e'}}{\tau_{esc}^{e'}} - \frac{N_{ES2}^e f_{WL}^{e'}}{\tau_{esc}^{e'}} - \frac{N_{ES2}^e f_{ES1}^{e'}}{\tau_0^e} - \frac{N_{ES2}^e}{\tau_{nr}^{e'}} \quad (5)$$

$$\frac{dN_{ES1}^e}{dt} = \frac{N_{ES2}^e f_{ES1}^{e'}}{\tau_0^e} + \frac{N_{GS}^e f_{ES1}^{e'}}{\tau_{esc}^{e'}} - \frac{N_{ES1}^e f_{ES2}^{e'}}{\tau_{esc}^{e'}} - \frac{N_{ES1}^e f_{GS}^{e'}}{\tau_0^e} - \frac{N_{ES1}^e}{\tau_{nr}^{e'}} \quad (6)$$

$$\frac{dN_{GS}^e}{dt} = \frac{N_{ES1}^e f_{GS}^{e'}}{\tau_0^e} - \frac{N_{GS}^e f_{ES1}^{e'}}{\tau_{esc}^{e'}} - \frac{N_{GS}^e}{\tau_{nr}^{e'}} - v_{gr} g S \cdot \frac{V_{AR} \Delta z}{L} \quad (7)$$

(3) – (7) describe the carrier numbers in a laser section  $w \times \Delta z$ , with  $w$  and  $\Delta z$  being the waveguide width and the space step discretizing the laser. The equations include carrier injection into the BL, carrier capture and cascaded relaxation into the QD ground states, thermal escape, and standard non-radiative recombination.  $f_n' = (1 - f_n)$  is the probability of finding an empty state in the energy level  $n$ . A modification of the QD equations with respect to dislocation loss is not required, as the relative number of QDs directly affected by TDs is very low. An explanation of all used symbols is given in Table I.

The hole BL and WL equations are analogous to (3) and (4), whereas the hole QD levels are modelled via one joint equation, as the holes thermalize among the various confined states due to their small energy spacing [37].

$$\frac{dN_{QD}^h}{dt} = \frac{N_{WL}^h f_{QD}^{h'}}{\tau_0} - \frac{N_{QD}^h f_{WL}^{h'}}{\tau_{esc}^{h'}} - \frac{N_{QD}^h}{\tau_{nr}^{h'}} - v_{gr} g S \cdot \frac{V_{AR} \Delta z}{L} \quad (8)$$

The gain  $g$  is then calculated as a function of the electron and hole occupation QD occupation probabilities, and the photon density  $S$  is computed using a pair of field equations [38].

Apart from the necessary modifications, the QW model is built as similar as the QD model as possible. The QW laser is simulated as a two-level system with BL and QWs, yielding

$$\frac{dN_{BL}^{e,h}}{dt} = \frac{\eta I \Delta z}{e L} + \frac{N_{QW}^{e,h} f_{BL}^{e,h'}}{\tau_{esc}^{e,h'}} - \frac{N_{BL}^{e,h} f_{QW}^{e,h'}}{\tau_c^{e,h'}} - \frac{N_{BL}^{e,h}}{\tau_{nr}^{e,h'}} - \frac{N_{BL}^{e,h}}{\tau_{dis}^{e,h}} \quad (9)$$

$$\frac{dN_{QW}^{e,h}}{dt} = \frac{N_{BL}^{e,h} f_{QW}^{e,h'}}{\tau_c^{e,h'}} - \frac{N_{QW}^{e,h} f_{BL}^{e,h'}}{\tau_{esc}^{e,h'}} - \frac{N_{QW}^{e,h}}{\tau_{nr}^{e,h'}} - \frac{N_{QW}^{e,h}}{\tau_{dis}^{e,h}} - v_{gr} g S \cdot \frac{V_{AR} \Delta z}{L} \quad (10)$$

The field equations can be adapted directly from the QD model, incorporating a standard logarithmic QW gain function [39].

The  $L$ - $I$  characteristics of QD and QW lasers are modelled as a function of the dislocation density. The QD laser parameters were chosen based on earlier simulations [38] and adjusted to

TABLE I PARAMETERS USED FOR QW AND QW SIMULATIONS SHOWN IN FIG. 5(A) AND (B).

QD parameters	QW parameters
Laser wavelength $\lambda_{QD} = 1310 \text{ nm}$	Laser wavelength $\lambda_{QW} = 980 \text{ nm}$
Modal gain $g_{mod} = 25 \text{ cm}^{-1}$	Gain constant $g_0 = 3000 \text{ cm}^{-1}$
Optical confinement factor $\Gamma = 0.005$	Optical confinement factor $\Gamma = 0.02$
Gain saturation factor $\varepsilon = 5 \times 10^{16} \text{ cm}^3$	Gain saturation factor $\varepsilon = 1 \times 10^{17} \text{ cm}^3$
QD degeneracies $p_i = 2, 4, 6, 6, 6$ (GS, ES1-ES4)	Transparency current density $n_0 = 1.6 \times 10^{18} \text{ cm}^{-3}$
QD carrier capture time $\tau_c^{QD,e,h} = 3 \text{ ps}, 0.5 \text{ ps}$	
Intradot relaxation time $\tau_0^e = 250 \text{ fs}$	
QD density $\rho = 4 \times 10^{10} \text{ cm}^{-2}$	
Thermal escape time $\tau_{esc}^{GS,ES1,ES2,e} = 1.6 \text{ ps}, 2.1 \text{ ps}, 3.7 \text{ ps}, \tau_{esc}^{QD,h} = 21.5 \text{ ps}$	
Parameters unchanged for QD and QW simulations:	
Laser length $L = 3 \text{ mm}$	Diffusion constant $D_{GaAs}^{e,h} = 191 \text{ cm}^2/\text{s}, 10 \text{ cm}^2/\text{s}$
Waveguide width $w = 50 \text{ }\mu\text{m}$	Diffusion constant $D_{InGaAs}^{e,h} = 176 \text{ cm}^2/\text{s}, 8 \text{ cm}^2/\text{s}$
Number of active layers $N_{layers} = 5$	Barrier layer current injection efficiency $\eta = 0.55$
WL/QW thickness: $h_{WL,QW} = 8 \text{ nm}$	WL/QW transport/capture time $\tau_c^{WL,e,h} = 6.4 \text{ ps}, 8.2 \text{ ps}$
BL thickness $h_{BL} = 40 \text{ nm}$	BL, WL/QW, and QD carrier lifetime $\tau_{nr}^{e,h} = 7 \text{ ns}$
Group velocity $v_{gr}$ , active region volume $V_{AR}$	Waveguide loss $\alpha_i = 3 \text{ cm}^{-1}$
Thermal escape time $\tau_{esc}^{WL/QW,e} = 3.3 \text{ ps}, \tau_{esc}^{WL/QW,h} = 2.3 \text{ ps}$	Facet reflectivities $R_1 = R_2 = 0.3$

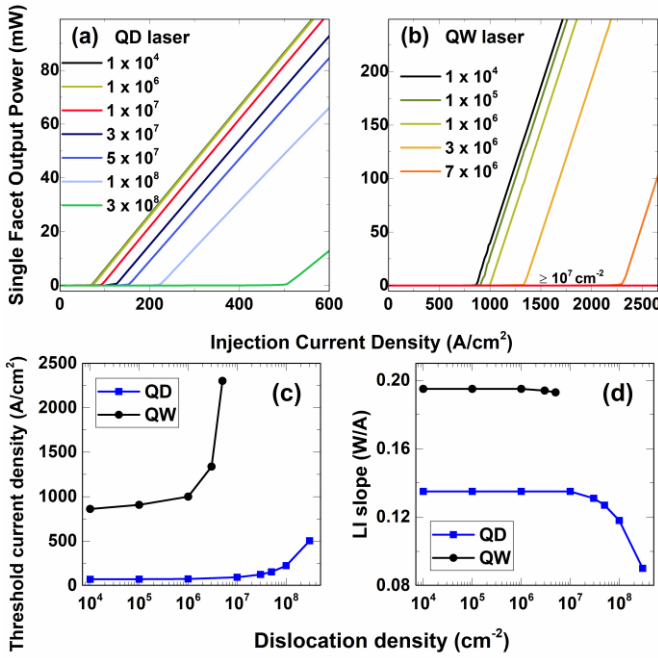


Fig. 5.  $L$ - $I$  curves calculated for an uncoated  $50 \mu\text{m} \times 3 \text{mm}$  QD (a) and QW laser (b) as a function of the dislocation density in  $\text{cm}^{-2}$ , using the simulation parameters shown in Table 1 and the introduced dislocation loss term. (c) and (d) show the respective threshold current densities and the  $L$ - $I$  slope.

reproduce the experimental  $L$ - $I$  curve, whereas the QW laser parameters are based on those in Ref. 39. The simulation results are shown in Fig. 5(a) and (b). From Fig. 5(a) it can be seen that very good QD lasing characteristics are obtained for TD densities between  $10^4 \text{ cm}^{-2}$  and  $10^6 \text{ cm}^{-2}$ . There is only a minor threshold current density increase from  $1 \times 10^6 \text{ cm}^{-2}$  to  $1 \times 10^7 \text{ cm}^{-2}$ , indicating that for these dislocation densities, which are typical values for III-V lasers grown on Si, the effect on the  $L$ - $I$  characteristics of a high-gain QD laser is limited. This finding agrees well with other reports of excellent performance of QD lasers grown on Si [12, 19]. As the dislocation density continues to rise, however, the threshold rises significantly, as can be seen in Fig. 5(c). From  $\rho_{dis} = 1 \times 10^8 \text{ cm}^{-2}$  to  $3 \times 10^8 \text{ cm}^{-2}$ , the threshold current density increases from  $225 \text{ Acm}^{-2}$  to  $500 \text{ Acm}^{-2}$  (330 mA and 760 mA, respectively). Furthermore, the increase in laser threshold is accompanied by a slope reduction of about 34 % from  $\rho_{dis} = 1 \times 10^4 \text{ cm}^{-2}$  to  $3 \times 10^8 \text{ cm}^{-2}$ , as shown in Fig. 5(d), since the high BL and WL carrier loss rate manifests itself effectively in a reduced injection efficiency into the QDs. These results agree with the experimentally observed trends reported by Jung et al. and Orchard et al. [30, 40]. It is, however, likely that the modelled slope decrease is even underestimated, since a very high TD density will also lead to dislocation-induced optical losses, as indicated in Ref. 40. Despite the performance reduction observed at higher values of  $\rho_{dis}$ , our theoretical results support the hypothesis that the unique properties of QDs, efficient carrier capture and high carrier confinement, are key to the impressive capabilities of QD lasers on Si to operate under high TD densities [30, 32]. It should be noted that our model does not contain thermal effects, so it is not considered that the possibility of overcoming the laser threshold may be reduced at increased injection levels.

The good qualitative agreement between theory and experiment enables us to apply our approach to the simulation of dislocation-dependent QW  $L$ - $I$  curves. Fig. 5 (c) reveals that an equivalent QW laser without QD energy level is more seriously affected by dislocation-induced carrier loss. The threshold current density required to pump a QW-based laser is naturally much higher, yet the threshold increases drastically at  $\rho_{dis} > 1 \times 10^6 \text{ cm}^{-2}$ . At a TD density of  $10^7 \text{ cm}^{-2}$ , no lasing is obtained within the chosen input currents. The finding that  $\sim 10^6 \text{ cm}^{-2}$  may be the highest tolerable ‘time-zero’ TD density for a QW laser correlates well with the defect densities measured for the few QW lasers grown on Si [41].

#### IV. CONCLUSION

In conclusion, we have presented a study on the effect of enhanced non-radiative recombination through threading dislocations (TDs) on the performance of InAs/GaAs QD and InGaAs/GaAs QW lasers monolithically grown on (001) Si in order to explain the much superior performance obtained with InAs/GaAs QD active regions rather than  $\text{In}_{0.15}\text{Ga}_{0.85}\text{As}/\text{GaAs}$  QWs. A high-performance InAs/GaAs QD laser monolithically grown on Si was demonstrated with a low cw threshold current density of  $173 \text{ Acm}^{-2}$ , high single-facet output power exceeding 100 mW, and a high operation temperature of  $105 \text{ }^\circ\text{C}$  under pulsed mode. In contrast, an InGaAs/GaAs QW laser with a similar TD density grown on Si substrate under identical conditions showed no lasing behavior at room temperature, confirming the advantages of QDs over QW-based active regions in lasers monolithically grown on Si [42]. These advantages are well explained by our model. QD structures benefit from efficient carrier capture into the QD states and high energy barriers, which prevent the carriers from migrating into defect states. For this reason, even at very high defect densities on the order of  $10^8 \text{ cm}^{-2}$ , QD lasers with high-gain active regions are able to show lasing, whereas the performance of QW lasers suffers significantly at lower TD densities of  $\sim 10^6 \text{ cm}^{-2}$ . Our phenomenological model is able to reproduce the trends published in the literature, where an increased TD density is accompanied by an increase of the threshold current and a reduction of the  $L$ - $I$  slope. Ignoring the effects of recombination enhanced defect reactions, dislocation climb, and the respective device lifetime issues, our simulations show that QW lasers are more severely affected by dislocation-induced carrier loss than QD lasers, meaning that the TD density may almost have to be reduced to the level of native substrates in order to produce well-functioning monolithic QW lasers on Si. The experimental and theoretical study presented here is a first approach to assessing how many dislocations may be tolerable for QD and QW laser active regions and make a significant contribution to understand high-performance III-V QD lasers monolithically grown on Si, and hence further enhance the performance of III-V/Si QD lasers for Si photonics.

#### REFERENCES

- [1] M. Asghari and A. V. Krishnamoorthy, "Energy-efficient communication," *Nature Photonics*, vol. 5, p. 268, 2011.

- [2] Y. A. Vlasov, "Silicon CMOS-integrated nano-photonics for computer and data communications beyond 100G," *IEEE Communications Magazine*, vol. 50, no. 2, pp. s67-s72, 2012.
- [3] D. Liang and J. E. Bowers, "Recent progress in lasers on silicon," *Nat Photon*, 10.1038/nphoton.2010.167 vol. 4, no. 8, pp. 511-517, 08/print 2010.
- [4] J. Liu, X. Sun, R. Camacho-Aguilera, L. C. Kimerling, and J. Michel, "Ge-on-Si laser operating at room temperature," *Optics Letters*, vol. 35, no. 5, pp. 679-681, 2010/03/01 2010.
- [5] S. Wirths et al., "Lasing in direct-bandgap GeSn alloy grown on Si," *Nat Photon, Letter* vol. 9, no. 2, pp. 88-92, 02/print 2015.
- [6] H. Rong et al., "An all-silicon Raman laser," *Nature*, 10.1038/nature03273 vol. 433, no. 7023, pp. 292-294, 01/20/print 2005.
- [7] G. Roelkens et al., "III-V/silicon photonics for on-chip and intra-chip optical interconnects," *Laser & Photonics Reviews*, vol. 4, no. 6, pp. 751-779, 2010.
- [8] Z. Wang et al., "A III-V-on-Si ultra-dense comb laser," *Light Sci Appl., Original Article* vol. 6, p. e16260, 05/19/online 2017.
- [9] B. Kunert, I. Németh, S. Reinhard, K. Volz, and W. Stolz, "Si (001) surface preparation for the antiphase domain free heteroepitaxial growth of GaP on Si substrate," *Thin Solid Films*, vol. 517, no. 1, pp. 140-143, 11/3/ 2008.
- [10] R. Alcotte et al., "Epitaxial growth of antiphase boundary free GaAs layer on 300 mm Si(001) substrate by metalorganic chemical vapour deposition with high mobility," *APL Materials*, vol. 4, p. 046101, 2016.
- [11] Y. Wan, Q. Li, Y. Geng, B. Shi, and K. M. Lau, "InAs/GaAs quantum dots on GaAs-on-V-grooved-Si substrate with high optical quality in the 1.3  $\mu\text{m}$  band," *Applied Physics Letters*, vol. 107, no. 8, p. 081106, 2015.
- [12] D. Jung et al., "High efficiency low threshold current 1.3  $\mu\text{m}$  InAs quantum dot lasers on on-axis (001) GaP/Si," *Applied Physics Letters*, vol. 111, no. 12, p. 122107, 2017.
- [13] S. Chen et al., "Electrically pumped continuous-wave 1.3  $\mu\text{m}$  InAs/GaAs quantum dot lasers monolithically grown on on-axis Si (001) substrates," *Optics Express*, vol. 25, no. 5, pp. 4632-4639, 2017/03/06 2017.
- [14] Y. Wang et al., "Monolithic quantum-dot distributed feedback laser array on silicon," *Optica*, vol. 5, no. 5, pp. 528-533, 2018.
- [15] M. Tang et al., "1.3- $\mu\text{m}$  InAs/GaAs quantum-dot lasers monolithically grown on Si substrates using InAlAs/GaAs dislocation filter layers," *Optics Express*, vol. 22, no. 10, pp. 11528-11535, 2014/05/19 2014.
- [16] S. Chen et al., "Electrically pumped continuous-wave III-V quantum dot lasers on silicon," *Nature Photonics*, vol. 10, p. 307, 03/07/online 2016.
- [17] M. Tang et al., "Optimizations of Defect Filter Layers for 1.3- $\mu\text{m}$  InAs/GaAs Quantum-Dot Lasers Monolithically Grown on Si Substrates," *IEEE Journal of Selected Topics in Quantum Electronics*, vol. 22, no. 6, pp. 50-56, 2016.
- [18] A. Y. Liu, R. W. Herrick, O. Ueda, P. M. Petroff, A. C. Gossard, and J. E. Bowers, "Reliability of InAs/GaAs Quantum Dot Lasers Epitaxially Grown on Silicon," *IEEE Journal of Selected Topics in Quantum Electronics*, vol. 21, no. 6, pp. 690-697, 2015.
- [19] D. Jung et al., "Highly Reliable Low-Threshold InAs Quantum Dot Lasers on On-Axis (001) Si with 87% Injection Efficiency," *ACS Photonics*, 2017/12/18 2017.
- [20] K. Böhm and B. Fischer, "Photoluminescence at dislocations in GaAs and InP," *Journal of Applied Physics*, vol. 50, no. 8, pp. 5453-5460, 1979.
- [21] B. Kunert, Y. Mols, M. Baryshnikova, N. Waldron, A. Schulze, and R. Langer, "How to control defect formation in monolithic III/V hetero-epitaxy on (100) Si? A critical review on current approaches," *Semiconductor Science and Technology*, vol. 33, no. 9, p. 093002, 2018.
- [22] R. Beanland, D. J. Dunstan, and P. J. Goodhew, "Plastic relaxation and relaxed buffer layers for semiconductor epitaxy," *Advances in Physics*, vol. 45, no. 2, pp. 87-146, 1996/04/01 1996.
- [23] Zaman I. Kazi, P. Thilakan, T. Egawa, M. Umeno, and T. Jimbo, "Realization of GaAs/AlGaAs Lasers on Si Substrates Using Epitaxial Lateral Overgrowth by Metalorganic Chemical Vapor Deposition," *Japanese Journal of Applied Physics*, vol. 40, no. 8R, p. 4903, 2001.
- [24] H. Deng et al., "III-V Quantum Dot Lasers Monolithically Grown on Silicon," in 2019 Optical Fiber Communications Conference and Exhibition (OFC), 2019, pp. 1-3.
- [25] H. Y. Liu et al., "Optimizing the growth of 1.3  $\mu\text{m}$  InAs/InGaAs dots-in-a-well structure," *Journal of Applied Physics*, vol. 93, no. 5, pp. 2931-2936, 2003.
- [26] Z. Y. Xu et al., "Carrier relaxation and thermal activation of localized excitons in self-organized InAs multilayers grown on GaAs substrates," *Physical Review B*, vol. 54, no. 16, pp. 11528-11531, 10/15/ 1996.
- [27] O. B. Shchekin, G. Park, D. L. Huffaker, and D. G. Deppe, "Discrete energy level separation and the threshold temperature dependence of quantum dot lasers," *Applied Physics Letters*, vol. 77, no. 4, pp. 466-468, 2000.
- [28] A. Y. Liu, S. Srinivasan, J. Norman, A. C. Gossard, and J. E. Bowers, "Quantum dot lasers for silicon photonics [Invited]," *Photonics Research*, vol. 3, no. 5, pp. B1-B9, 2015/10/01 2015.
- [29] J. S. Speck and S. J. Rosner, "The role of threading dislocations in the physical properties of GaN and its alloys," *Physica B: Condensed Matter*, vol. 273-274, pp. 24-32, 1999/12/15/ 1999.
- [30] D. Jung et al., "Impact of threading dislocation density on the lifetime of InAs quantum dot lasers on Si," *Applied Physics Letters*, vol. 112, no. 15, p. 153507, 2018.
- [31] S. A. Moore, L. O. Faolain, M. A. Cataluna, M. B. Flynn, M. V. Kotlyar, and T. F. Krauss, "Reduced surface sidewall recombination and diffusion in quantum-dot lasers," *IEEE Photonics Technology Letters*, vol. 18, no. 17, pp. 1861-1863, 2006.
- [32] H. Huang et al., "Analysis of the optical feedback dynamics in InAs/GaAs quantum dot lasers directly grown on silicon," *Journal of the Optical Society of America B*, vol. 35, no. 11, pp. 2780-2787, 2018/11/01 2018.
- [33] L. Chernyak, A. Osinsky, and A. Schulte, "Minority carrier transport in GaN and related materials," *Solid-State Electronics*, vol. 45, no. 9, pp. 1687-1702, 2001/09/01/ 2001.
- [34] W. R. Harding, I. D. Blenkinsop, and D. R. Wight, "Dislocation-limited minority-carrier lifetime in n-type GaP," *Electronics Letters*, vol. 12, no. 19, pp. 503-504

- [35] H. Y. Liu et al., "Improved performance of 1.3 $\mu$ m multilayer InAs quantum-dot lasers using a high-growth-temperature GaAs spacer layer," *Applied Physics Letters*, vol. 85, no. 5, pp. 704-706, 2004.
- [36] C. L. Andre et al., "Impact of dislocations on minority carrier electron and hole lifetimes in GaAs grown on metamorphic SiGe substrates," *Applied Physics Letters*, vol. 84, no. 18, pp. 3447-3449, 2004.
- [37] M. Gioannini and M. Rossetti, "Time-Domain Traveling Wave Model of Quantum Dot DFB Lasers," *IEEE Journal of Selected Topics in Quantum Electronics*, vol. 17, no. 5, pp. 1318-1326, 2011.
- [38] C. Hantschmann et al., "Gain Switching of Monolithic 1.3  $\mu$ m InAs/GaAs Quantum Dot Lasers on Silicon," *Journal of Lightwave Technology*, pp. 1-1, 2018.
- [39] M. G. Thompson, "Ultra-short pulse generation in quantum well and quantum dot monolithic mode-locked laser diodes," University of Cambridge, 2007.
- [40] J. R. Orchard et al., "In situ annealing enhancement of the optical properties and laser device performance of InAs quantum dots grown on Si substrates," *Optics Express*, vol. 24, no. 6, pp. 6196-6202, 2016/03/21 2016.
- [41] M. E. Groenert et al., "Monolithic integration of room-temperature cw GaAs/AlGaAs lasers on Si substrates via relaxed graded GeSi buffer layers," *Journal of Applied Physics*, vol. 93, no. 1, pp. 362-367, 2003.
- [42] M. Tang et al., "Integration of III-V lasers on Si for Si photonics," *Progress in Quantum Electronics*, 2019.(DOI: 10.1016/j.pquantelec.2019.05.002).